

An Early Diagnostics of the Geoeffectiveness of Solar Eruptions from Photospheric Magnetic Flux Observations: The Transition from SOHO to SDO

I.M. Chertok¹  · V.V. Grechnev²  · A.A. Abunin¹ 

Received: 29 June 2016 / Accepted: 14 March 2017
© Springer Science+Business Media Dordrecht 2017

Abstract In our previous articles (Chertok *et al.* in *Solar Phys.* **282**, 175, 2013; Chertok *et al.* in *Solar Phys.* **290**, 627, 2015), we presented a preliminary tool for the early diagnostics of the geoeffectiveness of solar eruptions based on the estimate of the total unsigned line-of-sight photospheric magnetic flux in accompanying extreme ultraviolet (EUV) arcades and dimmings. This tool was based on the analysis of eruptions observed during 1996–2005 with the *Extreme-ultraviolet Imaging Telescope* (EIT) and the *Michelson Doppler Imager* (MDI) onboard the *Solar and Heliospheric Observatory* (SOHO). Empirical relationships were obtained to estimate the probable importance of upcoming space weather disturbances caused by an eruption, which just occurred, without data on the associated coronal mass ejections. In particular, it was possible to estimate the intensity of a non-recurrent geomagnetic storm (GMS) and Forbush decrease (FD), as well as their onset and peak times. After 2010–2011, data on solar eruptions are obtained with the *Atmospheric Imaging Assembly* (AIA) and the *Helioseismic and Magnetic Imager* (HMI) onboard the *Solar Dynamics Observatory* (SDO). We use relatively short intervals of overlapping EIT–AIA and MDI–HMI detailed observations, and additionally, a number of large eruptions over the next five years with the 12-hour cadence EIT images to adapt the SOHO diagnostic tool to SDO data. We show that the adopted brightness thresholds select practically the same areas of arcades and dimmings from the EIT 195 Å and AIA 193 Å image, with a cross-calibration factor of 3.6–5.8 (5.0–8.2) for the AIA exposure time of 2.0 s (2.9 s). We also find that for the same photospheric areas, the MDI line-of-sight magnetic flux systematically exceeds the

Earth-Affecting Solar Transients

Guest Editors: Jie Zhang, Xochitl Blanco-Cano, Nariaki Nitta, and Nandita Srivastava

✉ I.M. Chertok
ichertok@izmiran.ru

V.V. Grechnev
grechnev@iszf.irk.ru

A.A. Abunin
abunin@izmiran.ru

¹ Pushkov Institute of Terrestrial Magnetism, Ionosphere and Radio Wave Propagation (IZMIRAN), Troitsk, Moscow 108840, Russia

² Institute of Solar-Terrestrial Physics SB RAS, Lermontov St. 126A, Irkutsk 664033, Russia

HMI flux by a factor of 1.4. Based on these results, the empirical diagnostic relationships obtained from SOHO data are adjusted to SDO instruments. Examples of a post-diagnostics based on SDO data are presented. As before, the tool is applicable to non-recurrent GMSs and FDs caused by nearly central eruptions from active regions, provided that the southern component of the interplanetary magnetic field near the Earth is predominantly negative, which is not predicted by this tool.

Keywords Solar eruptions · Coronal mass ejections · Dimmings · Arcades · Magnetic flux · Forbush decreases · Geomagnetic storms

1. Introduction

Coronal mass ejections (CMEs) and their interplanetary counterparts, interplanetary coronal mass ejections (ICMEs), and in particular magnetic clouds, are prime drivers of the most severe non-recurrent space weather disturbances. Most significant among them are major geomagnetic storms (GMSs) (*e.g.* Gosling, 1993; Bothmer and Zhukov, 2007; Gopalswamy, Tsurutani, and Yan, 2015) and Forbush decreases (FDs) of the intensity of galactic cosmic rays (Cane, 2000; Belov, 2009; Richardson and Cane, 2011). One of the most important challenges of solar-terrestrial physics and space weather prediction is the diagnostics of the geoefficiency of CMEs, *i.e.* an approximate estimation and forecast of possible non-recurrent GMS and FD parameters from observed characteristics of an eruption that has just occurred. On the Sun, CME eruptions are accompanied by phenomena such as bright post-eruption arcades (Kahler, 1977; Sterling *et al.*, 2000; Hudson and Cliver, 2001; Tripathi, Bothmer, and Cremades, 2004; Yashiro *et al.*, 2013) and large-scale dark dimmings (Thompson *et al.*, 1998; Hudson and Cliver, 2001; Harra *et al.*, 2011). They are observed particularly in the extreme-ultraviolet (EUV) range and represent the structures and areas involved in the CME process.

Our previous articles (Chertok *et al.*, 2013, 2015 hereafter referred to as Article I and Article II) showed the total unsigned magnetic flux of the longitudinal field at the photospheric level within the arcade and dimming areas to be a suitable quantitative parameter for the earliest diagnostics of the geoefficiency of solar eruptions. This approach is based on widely accepted concepts relating paired core dimmings to the footpoints of an erupting CME flux rope and the post-eruption arcade to the magnetic structures remaining after reconnection that formed this flux rope. We studied events of Solar Cycle 23 during 1996–2005, in which sources of major non-recurrent GMSs with a geomagnetic index $Dst < -100$ nT were reliably identified as near disk-center active regions (ARs). These eruptions were analyzed using data from the *Solar and Heliospheric Observatory* (SOHO: Domingo, Fleck, and Poland, 1995), namely solar images obtained with the *Extreme-ultraviolet Imaging Telescope* (EIT: Delaboudinière *et al.*, 1995) in the 195 Å channel and magnetograms acquired with the *Michelson Doppler Imager* (MDI: Scherrer *et al.*, 1995). As a result, clear correlations were found between the erupted magnetic flux below the arcades and dimmings following eruptions from ARs and the amplitude of GMSs (Dst and A_p indexes) and FDs, as well as their temporal parameters (intervals between the solar eruptions and the GMS onset and peak times). The higher the erupted flux, the stronger the GMS or FD intensities and the shorter the ICME transit time. These correlations indicate that the quantitative characteristics of major non-recurrent space weather disturbances are largely determined by measurable parameters of solar eruptions, in particular by the magnetic flux within the arcade and dimming areas, and can be tentatively estimated in advance with a lead time from one to four days.

These dependencies expressed in corresponding empirical relationships constitute a preliminary tool based on SOHO data for an early diagnostics of geoefficiency of solar eruptions and a short-term forecasting of the main parameters of non-recurrent space weather disturbances. However, at the end of 2010 July, the synoptic 12-min cadence SOHO/EIT observations in the 195 Å channel were replaced by obtaining only two images *per* day, at around 01:13 and 13:13 UT (see the EIT catalog at <http://umbra.nascom.nasa.gov/eit/eit-catalog.html>). In addition, the solar magnetic field observations with the SOHO/MDI magnetograph were terminated in 2011 April (see the MDI Daily Magnetic Field Synoptic Data at <http://soi.stanford.edu/magnetic/index5.html>).

Solar activity in the current Cycle 24 is relatively low. This has resulted in a smaller number of non-recurrent geospace disturbances initiated by eruptions from ARs that were relatively weak (Gopalswamy, Tsurutani, and Yan, 2015). For this reason, it is not possible to repeat the analysis of Articles I and II for the data of the *Solar Dynamic Observatory* (SDO: Pesnell, Thompson, and Chamberlin, 2012), which provides regular high-quality observations starting in early 2010 May. To use our tool at the present time for the early diagnosis of solar eruptions, our procedures need to be upgraded for the usage of SDO data. To correctly shift from SOHO data to SDO, we examine our diagnostic tool using both SOHO and SDO observations in the intervals when they overlap. To extract the arcade and dimming areas, it is now reasonable to use the SDO *Atmospheric Imaging Assembly* (AIA: Lemen *et al.*, 2012) images produced in the 193 Å channel instead of the SOHO/EIT 195 Å images, because both EUV channels have a close temperature response with peaks at about 1.3–1.5 MK. The magnetic flux in the extracted areas needs to be calculated with data from the SDO *Helioseismic and Magnetic Imager* (HMI: Scherrer *et al.*, 2012). These issues are the subject of the present article.

2. Data and Methodical Issues

Our approach invokes a widely accepted view of the flux rope formation in solar eruptions that is due to reconnection during flares. Conjugate footpoints of an erupted flux rope are revealed by paired core dimmings (Hudson and Cliver, 2001). Observational studies confirm this view (see, *e.g.*, Qiu *et al.*, 2007; Miklenic, Veronig, and Vršnak, 2009). In particular, Qiu *et al.* (2007) established for several events a quantitative correspondence between the flare-reconnected magnetic flux with the poloidal (azimuthal) flux in the corresponding magnetic clouds near Earth. A smaller toroidal (axial) flux corresponded to the magnetic flux in dimmed regions.

Any erupting structure initially has magnetically conjugate bases, even if it eventually becomes disconnected from the Sun. The magnetic flux in one base is expected to be the same throughout the erupting structure and in the conjugated base, *i.e.* the positive and negative magnetic fluxes are expected to be exactly balanced. A corresponding photospheric magnetogram presents numerous footpoints of compact loops along with the bases of the erupting structure. These footpoints are not involved in the eruption. The magnetic flux computed from a photospheric magnetogram therefore basically is excessive. To approach a real erupted magnetic flux, magnetic fields need to be extrapolated into the corona. Qiu *et al.* (2007) extrapolated magnetic fields to a fixed height of 2 Mm and calculated the signed flux in opposite-polarity regions separately. The flux balance defined as a ratio of the positive to negative flux ranged typically between 0.8 and 1.5. In a case study of Uralov *et al.* (2014), the flux balance was reached by adjusting the height of the extrapolation, and the ultimate result corresponded well to the estimations for the near-Earth magnetic cloud.

The last way (possibly in an elaborated form) appears to be the most promising for accurate estimates of the erupted magnetic flux. However, this laborious way is difficult to use in statistical studies such as Article I presented. To expedite calculations, we directly measure in this article the magnetic flux from photospheric magnetograms, without extrapolation. The balanced conjugate bases of erupting structures are not known in this situation, and we use unsigned magnetic fluxes below arcades and dimming regions for simplicity and consistency with Articles I and II. Such measurements overestimate a real erupted flux by a factor of two because we sum the outgoing and incoming fluxes. Our direct measurement of the magnetic flux from the photospheric magnetograms without extrapolation causes an additional overestimate by a factor varying from one event to another. Thus, the actual flux in a magnetic cloud is presumably less than our estimates by a factor of 4–10. A constant factor does not affect the statistical patterns we discuss, and an unknown variable factor contributes to the scatter, along with other circumstances that we do not consider, such as the sign of the southern component of the interplanetary magnetic field, B_z , the presence of a possible negative B_z in the leading or trailing part of a magnetic cloud, and others.

We extract arcades and dimmings in EIT and AIA images with the same techniques as those used in Article I, based on formal criteria referring to a brightness analysis, as described below. These criteria detect the features of interest more or less reliably; nevertheless, manual assistance in the interactive mode is generally required to include separate disconnected regions or to eliminate irrelevant regions in full-disk images.

To facilitate interactive manipulations, we reduce both EIT and AIA images by rebinning them to a common format of 512×512 pixels, as we previously handled SOHO data (Article I). Most EIT images and all MDI magnetograms have 1024×1024 pixels; we decrease their resolution by a factor of two. Sometimes, EIT images are produced in a binned form of 512×512 pixels; then, these are unchanged. SDO/AIA and HMI images have 4096×4096 pixels; their resolution is decreased by a factor of eight. Our analysis does not require full-resolution data, an advantage of reduced images is a slightly enhanced signal-to-noise ratio and a smaller contribution from compact defects.

The pixel size of the full-resolution SOHO/EIT images is $2.63''$. SOHO is located at the L1 Lagrangian point 0.01 AU sunward from the Earth. The EIT pixel size converted to the near-Earth vantage point of SDO is $2.63'' \times 0.99 = 2.604''$. The ratio of the linear scales in the EIT and AIA ($0.6''$ pixel size) images reduced to the 512×512 pixels format is $(2.604'' \times 2)/(0.60'' \times 8) = 1.085$. We also resize MDI magnetograms to match the reduced EIT images with a pixel size of about $5.2''$ and HMI magnetograms to match the reduced AIA images with a pixel size of $4.8''$. We refer henceforth to the reduced images (512×512 pixels) with these parameters.

The data processing was carried out with IDL employing SolarSoftware general-purpose and instrument-specific routines, as well as a library and special software developed by the authors for the present study. Required SOHO/EIT 195 Å and SDO/AIA 193 Å FITS files were downloaded from the NASA Solar Data Analysis Center and Joint Science Operations Center catalogs (<http://umbra.nascom.nasa.gov/eit/eit-catalog.html> and <http://jsoc2.stanford.edu/data/aia/synoptic/>). EIT images were processed by the standard EIT_PREP routine, and we handled level 1.5 AIA images without any additional pre-processing. We only normalized all AIA images observed during each event to a common exposure time, given by a pre-event image. The solar rotation in the analyzed images was removed and a background pre-eruption image was subtracted from each subsequent image to obtain fixed-base difference images.

For arcades, a criterion turned out to be appropriate that extracted the area around the flare site, where the brightness exceeded 5% of the maximum over the Sun during the event

(in an image with the brightest flare emission). This criterion is based on a relative brightness threshold and has been used for both EIT and AIA images without any adjustment.

The detection of dimming regions is more complex. Parameters of dimmings were computed from the so-called “portrait”, which shows in a single composite image all dimmings appearing during the event. The “dimming portrait” is generated by finding a minimum brightness in each pixel over the entire fixed-base difference set (see Chertok and Grechnev, 2005). Reinard and Biesecker (2008, 2009) concluded that dimmings only appeared in events associated with fast CMEs and strong flares. Thresholding of difference images by a certain value (say, -50 for EIT images) indeed reliably detects dimmings in flare-related eruptions from active regions, where pre-eruptive structures are bright, but can be insufficient in non-flare-related events outside of active regions, where the brightness of pre-eruptive structures is modest. To detect dimmings in these latter events, where depressions are generally shallower, the relative brightness thresholding is more efficient. A brightness depression deeper than -40% of a pre-event level is an optimal criterion for extraction of significant core dimmings located near the eruption center and obviously related to the eruption. On the other hand, this criterion is too strong for some flare-related eruptions. We therefore had to use a combined dimming-detecting criterion based on both relative and absolute thresholds; the latter are not the same for EIT and AIA because their sensitivity is different.

The difference in the sensitivity of the EIT and AIA telescopes can be compensated using the ratio of the AIA to EIT responses when both telescopes observe the same structure. Counts *per pixel* in an AIA image divided by this ratio (cross-calibration factor, CCF) are expected to be close to those in a corresponding EIT image, and both relative and absolute thresholds can be used for any image independent of the instrument that produced it.

We calculated the CCF for each event as the ratio of the AIA and EIT differences between the brightness of the quiet Sun and that of the sky, *i.e.* $CCF = (B_{qs} - B_{sky})_{AIA} / (B_{qs} - B_{sky})_{EIT}$. These levels were evaluated as the positions of the peaks of the histograms representing the brightness distributions (number of pixels *vs.* brightness represented by the counts *per pixel*) in the EIT and AIA images within a disk of $0.97R_{\odot}$ (quiet Sun) and outside $1.03R_{\odot}$ (sky) from the Sun center. The peaks are centered at the highest-probability values, around which pixels with a highest occurrence frequency are concentrated.

The pixels corresponding to bright structures fall in the quiet-Sun histogram considerably to the right of the peak, and those corresponding to dark coronal holes fall left of the peak. Statistical contributions of the bright and dark structures determined by their relative areas with respect to the solar disk are relatively small, and they do not displace the peak of the histogram. Similarly, bright off-limb structures do not affect the position of the peak corresponding to the sky level. This reliable technique has been widely used for calibration of microwave images produced by radio heliographs (*e.g.* Hanaoka *et al.*, 1994; Grechnev *et al.*, 2003; Kochanov *et al.*, 2013).

The brightness of the sky, B_{sky} , is close to zero in both EIT images pre-processed with the EIT_PREP routine and level 1.5 AIA images. Thus, dividing an AIA image by the CCF brings it to the EIT data range.

3. Comparison of Areas Involved in Eruptions

First, it is necessary to compare the configurations and areas of dimmings and arcades extracted for the same events in the SOHO/EIT 195 \AA and SDO/AIA 193 \AA images. Two groups of eruptions from the central part of the solar disk (mainly within $\pm 30^\circ$, sometimes

$\pm 45^\circ$ from the disk center) observed simultaneously with SOHO and SDO are considered (Table 1). Group A includes relatively weak eruptions in 2010 May–July for which EIT images observed with a detailed 12-minute interval were still available. Because of the low solar activity at that time, the events were selected by inspecting daily EIT and AIA movies showing signs of an eruption regardless of the importance and nature of the accompanying soft X-ray flares. A number of them were classified as filament eruptions outside ARs, although ultimately we are interested in eruptions from ARs. In contrast, Group B consists of evident, strong eruptions associated with flares of importance larger than M1.0 that occurred during 2011–2015. For these events we are forced to use the EIT images available with a 12-hour interval and cotermporal AIA images. Considering lifetimes of arcades and dimmings of several hours, an additional requirement for these events was that the GOES peak of the corresponding X-ray flares occurred not earlier than three hours before the EIT observational time, which is usually at 01:13 and 13:13 UT. An event was also required to be isolated in the sense that in the considered 12-hour interval between two EIT images there were no other events of a comparable intensity.

In most cases of Group A, an interval starting short before the eruption onset and lasting 3–4 hours afterward was considered, *i.e.* a set of 15–20 images was analyzed. During this interval, the main arcades and dimmings were already fully formed. For events of Group B, the first image was subtracted from the second one to reveal the arcades and dimmings in the difference image. In some events of Group B, the time of the second image was close to the time of the maximum of the corresponding soft X-ray flare.

As is known, the area of a post-eruption arcade increases with time. To avoid ambiguity, we therefore extracted an arcade area in events of Group A in an image that is temporally close to the maximum of the EUV flux from the selected area. Usually, this time is close to the peak time of a corresponding GOES soft X-ray flare or somewhat later. It is clear that for Group B events the extraction time was defined by the timing of the second EIT image, and most often, it did not correspond to the maximum dimming and arcade areas for the given event.

Table 1 lists eruptions of Groups A and B selected for comparison of the arcade and dimming areas in the EIT 195 Å and AIA 193 Å images. Each event is specified by its number with an index A or B in the first column, date in the second column, time in the third column of an image used for the arcade measurement for Group A and the soft X-ray flare peak time for Group B, GOES class of the related flare in the fourth column, and an approximate position of an eruption or flare in the fifth column. We do not present the exposure times (τ_{exp}) of the analyzed EIT images that are given in the headers of the corresponding FITS files, because almost all EIT images (except for those for two events) had $\tau_{\text{exp}} \approx 12.6$ s. As for the AIA pre-flare images, $\tau_{\text{exp}} \approx 2.9$ and 2.0 s are typical in the events from Groups A and B, respectively. Below we correct all AIA images for the exposure times to these two typical τ_{exp} , although some images of Group B events corresponding to the flare peaks were produced with a much shorter exposure time of up to $\tau_{\text{exp}} \approx 0.07$ s.

The results of calculating the CCF for all events and for two AIA exposure times typically used without flares are presented in the sixth column of Table 1 (separated by a slash for $\tau_{\text{exp}} = 2.0$ s and $\tau_{\text{exp}} = 2.9$ s) and in Figure 1, where the event number with an index of A or B is specified along the horizontal axis. For AIA $\tau_{\text{exp}} \approx 2.0$ s, the CCF varies in different events within a span of 3.6–5.8 and for $\tau_{\text{exp}} \approx 2.9$ s within a range of 5.0–8.2. A tendency is visible of some decrease in the CCF with time on a scale of several years; events with the smallest factor occurred in 2014–2015. The exceptions are two Group A events, events 7 and 8, which were observed on 2010 June 29 and in which the CCF was as small as 0.9–1.4. EIT produced in these events higher-sensitivity 512×512 pixel images, while its images had 1024×1024 pixels in all other events. The CCF is expected to

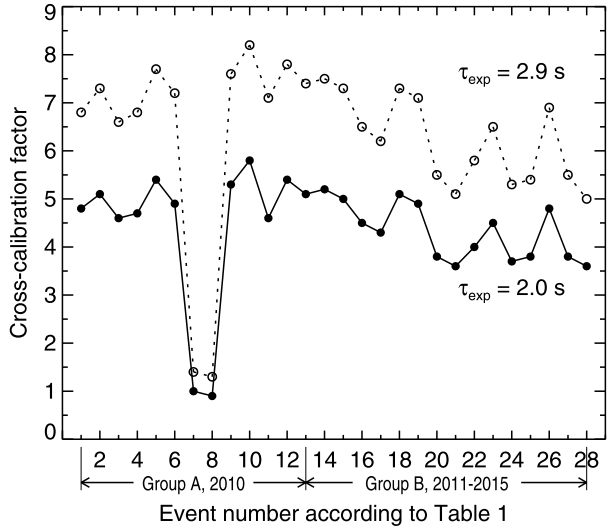
Table 1 Analyzed eruptions, a cross-calibration factor (CCF) between the EIT and AIA images, and areas of the extracted dimmings (Dim) and arcades (Arc).

No	Date	Time UT	GOES class	Position	CCF for τ_{exp} 2.0/2.9 s	SOHO/EIT area [pixels]		SDO/AIA area [pixels]	
						Dim	Arc	Dim	Arc
1A	2010-05-23	19:35	B1.3	N18W15	4.8/6.8	1828	761	1981	690
2A	2010-05-24	15:48	B1.1	N18W27	5.1/7.3	1131	306	1222	384
3A	2010-05-31	22:24	A6.5	N25W27	4.6/6.6	1095	414	1303	363
4A	2010-06-07	19:48	B2.0	N22E26	4.7/6.8	119	75	113	48
5A	2010-06-12	01:14	M2.0	N23W43	5.4/7.7	205	19	218	45
6A	2010-06-17	11:12	B5.0	N28E41	4.9/7.2	48	210	51	218
7A	2010-06-29	13:47	A5.0	S20W22	1.0/1.4	413	375	625	477
8A	2010-06-29	16:23	B1.3	N17W20	0.9/1.3	69	94	65	68
9A	2010-07-14	12:48	C1.4	N21E06	5.3/7.6	0	419	0	325
10A	2010-07-16	15:48	B1.3	S21W22	5.8/8.2	922	49	875	44
11A	2010-07-17	18:23	C2.4	N20W33	4.6/7.1	1496	97	1419	109
12A	2010-07-18	07:12	B1.0	N30E20	5.4/7.8	206	147	242	336
13A	2010-07-19	09:23	B4.0	N30W05	5.1/7.4	1316	267	1332	262
14B	2011-09-06	22:20	X2.1	N14W18	5.2/7.5	1395	276	1140	289
15B	2012-06-13	13:17	M1.2	S16E18	5.0/7.3	1054	253	984	203
16B	2012-08-11	12:20	M1.0	S28W38	4.5/6.5	544	487	639	451
17B	2013-08-12	10:41	M1.5	S17E19	4.3/6.2	249	118	242	189
18B	2013-10-13	00:43	M1.7	S22E17	5.1/7.3	1126	111	1170	79
19B	2013-10-24	00:30	M9.3	S10E08	4.9/7.1	1783	80	1820	62
20B	2014-01-07	10:13	M7.2	S13E11	3.8/5.5	0	765	0	821
21B	2014-02-04	01:23	M3.8	N09W13	3.6/5.1	50	116	54	79
22B	2014-04-18	13:03	M7.3	S18W37	4.0/5.8	303	241	600	177
23B	2014-10-24	21:41	X3.1	S16W21	4.5/6.5	0	733	45	742
24B	2015-03-11	00:02	M2.9	S16E28	3.7/5.3	321	105	302	124
25B	2015-03-15	23:22	M1.2	S17W35	3.8/5.4	273	402	306	336
26B	2015-03-16	10:58	M1.6	S17W39	4.8/6.9	134	468	149	564
27B	2015-06-21	01:42	M2.0	N12E13	3.8/5.5	238	342	263	242
28B	2015-11-09	13:12	M3.9	S11E41	3.6/5.0	137	131	321	83

be directly proportional to the AIA exposure time, *i.e.* $\text{CCF}(\tau_{\text{exp}} = 2.9)/\text{CCF}(\tau_{\text{exp}} = 2.0)$ is expected to be equal to $2.9/2.0 = 1.450$. The actual average ratio of the CCF for the two exposure times is 1.440 ± 0.027 , which characterizes the accuracy of our cross-calibration technique.

For each event we extracted the arcades and dimmings in the images produced with both EIT and AIA and compared their characteristics, including their quantitative areas. In the case of the AIA images, this was done for two combinations of the exposure times (2.0 and 2.9 s) and corresponding CCF. As noted in Section 2, in the images reduced to the same common format of 512×512 pixels, the AIA pixel size exceeds the corresponding EIT parameter by a factor of 1.085. In this study the dimming and arcade areas are expressed in

Figure 1 Cross-calibration factor (CCF) between the EIT 195 Å and AIA 193 Å images with an AIA exposure time of 2.0 and 2.9 s for Group A and B events labeled by sequential numbers as indicated in Table 1.



pixels. Consequently, to bring the AIA areas to the EIT scale, the AIA areas were divided by a factor $(1.085)^2 \approx 1.18$.

One of the main results is that the areas of the arcades and dimmings calculated from the AIA data practically do not change with these two combinations of exposure times and CCF. In the ninth and tenth columns of Table 1, the AIA dimming and arcade areas brought to the EIT pixel scale and those extracted from the EIT images (seventh and eighth columns) are presented. The corresponding scatter plots are shown in Figure 2. The majority of points corresponding to the EIT and AIA dimmings (Figure 2a) and arcades (Figure 2b) lie near the dotted bisector ($y = x$) line, which also nearly coincides with the best linear fit with a correlation coefficient of 0.98 for the dimmings and 0.95 for the arcades. We pay special attention to two events with a relatively large difference between the EIT and AIA dimming areas (event 22B) and arcade area (event 12A). Event 12A occurred almost without any enhancement in the soft X-ray flux, which stayed at the B1 background level. Accordingly, its arcade was very faint, and based on the accepted criteria, was extracted as small separate fragments. In event 22B, the scarcely extracted weak dimmings had a similar fragmentary character.

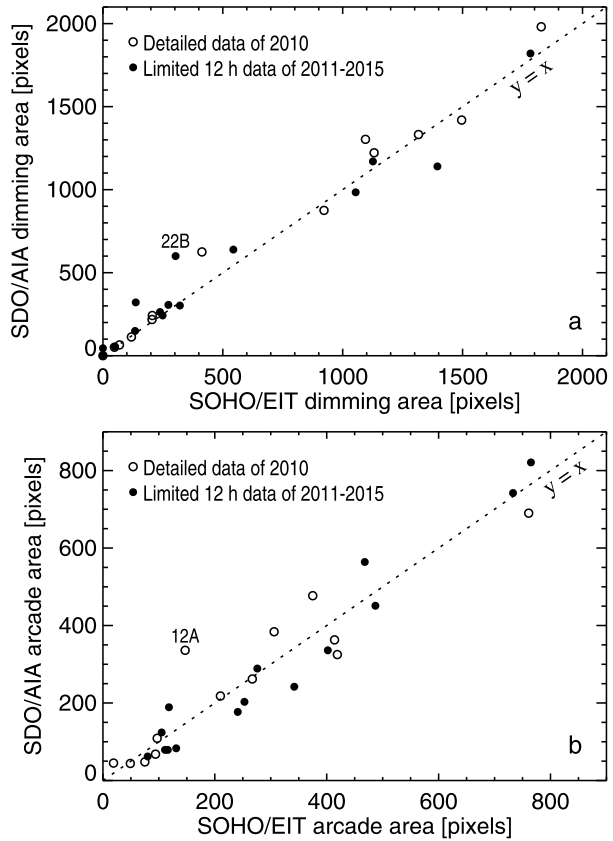
Another important result is that the extracted arcades and dimmings in practically all analyzed events coincide in the EIT and AIA images both in their areas and configurations. This is illustrated in Figure 3, where the close contours of the EIT and AIA dimmings and arcades of two Group A eruptions are presented by different colors on the background of the SDO/HMI pre-event magnetograms (bottom). The AIA difference images are very similar to those shown in Figures 3a and 3b.

All of these comparisons provide the basis for the general conclusion that with the adopted criteria, our procedures extract in the SDO/AIA 193 Å images the same dimmings and arcades as in the SOHO/EIT 195 Å images, and AIA data can be used instead of EIT.

4. Comparison of Erupted Magnetic Fluxes

The second procedure we considered is the comparison of the erupted magnetic fluxes as measured by the SOHO/MDI and SDO/HMI magnetographs. In the period between the

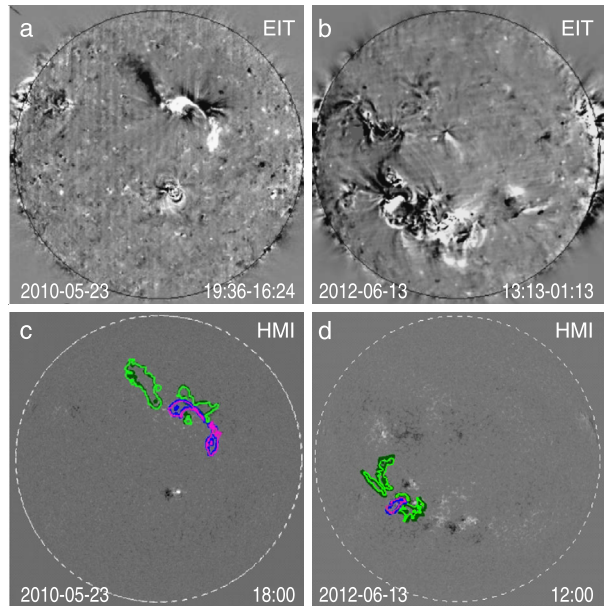
Figure 2 Scatter plots of (a) dimming and (b) arcade areas extracted in the EIT 195 Å and AIA 193 Å images. The AIA areas are brought to the EIT pixel scale. Open and filled circles denote events of Groups A and B, respectively. The dotted lines correspond to the equal areas ($y = x$).



beginning of HMI observations in 2010 May and end of MDI observations in 2011 April, there were no large eruptions in ARs. Moreover, many of the Group A events considered in the preceding section were associated with filament eruptions outside ARs and had very small magnetic fluxes. It is not reasonable to compare the MDI and HMI fluxes of these eruptions. Instead, we compare the total magnetic fluxes of the 34 largest ARs that were observed near the solar disk center during the concurrent MDI and HMI observations and had sunspot areas greater than 100 millionths of the Sun visible hemisphere (μHem) (see, *e.g.*, the Solar Monitor site <https://www.solarmonitor.org>). Although the measurements with HMI and MDI have been compared previously, *e.g.* by Liu *et al.* (2012), we are not aware of such comparisons for magnetic fluxes that erupted from large developed active regions, where magnetic fields are strong and saturation-like distortions are probable.

The observation date, time, NOAA number, coordinates, and maximum areas of these ARs are listed in Table 2. For each of these ARs, using data from both magnetographs, we calculated the total unsigned magnetic flux from the line-of-sight photospheric field within a single topologically connected area, where the magnetic field strength exceeded 10% of the maximum value over the entire magnetogram, but was not less than 15 G. All full-disk magnetograms were reduced to the 512×512 pixel format. For MDI we used level 1.8 magnetograms recalibrated in 2008 December. The corresponding MDI and HMI FITS files were downloaded from the Stanford University sites of the MDI Daily Magnetic Field Synop-

Figure 3 Top: bright post-eruption arcades and dark dimmings in SOHO/EIT 195 Å difference images for eruptions 1A (2010 May 23, panel a) and 15B (2012 June 13, panel b). Bottom: corresponding SDO/HMI pre-event magnetograms (panels c and d) overlaid with contours of extracted dimmings (dark green for AIA and light green for EIT) and arcades (blue for AIA and pink for EIT). The contours illustrate the acceptable correspondence between the areas selected from the images produced by the two instruments.



tic Data (<http://soi.stanford.edu/magnetic/index5.html>) and from the Stanford Joint Science Operations Center (<http://jsoc2.stanford.edu/data/hmi/fits/>).

The relationship between the MDI, Φ_{MDI} , and HMI, Φ_{HMI} , AR magnetic fluxes calculated in this way is shown in Figure 4. Its best linear fit in a wide range of the flux values of $\Phi_{\text{MDI}} \simeq 35\text{--}350$ and $\Phi_{\text{HMI}} \simeq 30\text{--}270$ (in 10^{20} Mx units) is $\Phi_{\text{MDI}} = (3.1 \pm 3.5) + (1.38 \pm 0.03)\Phi_{\text{HMI}}$ with a correlation coefficient of $r \approx 0.99$. Within the measurement errors, the factor we obtained from the analysis of the magnetic flux of ARs is consistent with the result of Liu *et al.* (2012), who established by a pixel-by-pixel comparison that the line-of-sight pixel-averaged magnetic signal inferred from MDI magnetograms was greater than that derived from the HMI data by the same scaling factor of 1.4. A close factor of 1.35 was also found by Svalgaard and Sun (2016). The differences between the measurements from MDI and HMI data can be due to their different calibration and a number of other factors (see Riley *et al.*, 2014; Watson, Penn, and Livingston, 2014; Couvidat *et al.*, 2016). Thus, in the transition from SOHO to SDO data, the relation $\Phi_{\text{MDI}} = 1.4\Phi_{\text{HMI}}$ should be used.

5. Transition Procedure

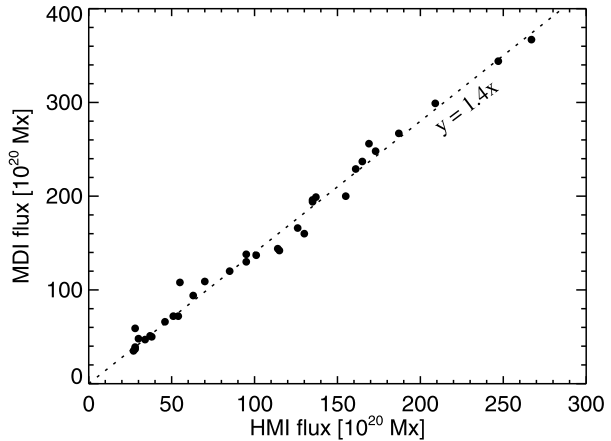
The results of the two previous sections allow us to adapt the SOHO diagnostic tool presented in Articles I and II to SDO data and current measurements. The updated tool does not need SOHO data. For the extraction of dimming and arcade areas for a particular eruption, it is sufficient to apply the cross-calibration factor between the EIT 195 Å and AIA 193 Å images. It is possible to simply adopt $\text{CCF} \approx 5$ for $\tau_{\text{exp}} \approx 2.0$ or $\text{CCF} \approx 7$ for $\tau_{\text{exp}} \approx 2.9$, based on Figure 1 for the first years. After that, one should download a FITS file of the HMI magnetogram that precedes the onset of an eruption and a number of AIA files covering approximately the duration of an associated soft X-ray flare. By analogy with the SOHO diagnosis, to extract the SDO dimmings and arcades, it is sufficient to take the AIA files with a

Table 2 The SOHO/MDI and SDO/HMI magnetic fluxes of the largest ARs over the period from 2010 May to 2011 April.

Date	Time hh, UT	AR number	Position	Area [μHem]	Magnetic flux [10^{20} Mx]	
					Φ_{MDI}	Φ_{HMI}
2010-05-24	08	11072	S15W23	130	94	63
2010-06-04	08	11076	S27W42	190	72	51
2010-07-04	08	11084	S19W33	150	35	27
2010-07-13	08	11087	N12E16	130	256	169
2010-07-22	08	11089	S24E32	310	144	114
2010-08-02	00	11092	N13E07	290	109	70
2010-08-07	08	11093	N12E31	180	72	54
2010-08-30	08	11101	N12W07	140	66	46
2010-09-17	08	11106	S20W09	110	229	161
2010-09-20	08	11108	S30E22	420	142	115
2010-09-28	08	11109	N22W12	420	248	173
2010-10-17	08	11112	S18W42	120	120	85
2010-10-18	08	11113	N18E09	160	47	34
2010-10-20	08	11115	S29W01	190	48	30
2010-10-28	00	11117	N22W42	450	237	165
2010-11-02	08	11120	N39E28	120	51	37
2010-11-16	08	11124	N14W44	260	137	101
2010-12-01	08	11130	N12W41	190	130	95
2010-12-08	08	11131	N31W11	430	166	126
2010-12-09	08	11133	N14E04	120	160	130
2011-01-02	08	11141	N35W38	100	39	28
2011-01-05	08	11140	N34E01	210	108	55
2011-02-16	08	11158	S21W41	600	267	187
2011-02-19	08	11162	N18W20	260	299	209
2011-02-21	08	11161	N11W42	260	199	137
2011-02-27	08	11163	N18E32	110	59	28
2011-03-05	08	11164	N25W33	570	367	267
2011-03-11	16	11166	N09W40	750	344	247
2011-03-13	08	11169	N19W36	260	196	135
2011-03-24	16	11176	S15E44	490	200	155
2011-03-27	08	11178	S15E29	130	50	38
2011-03-31	11	11183	N15E13	330	194	135
2011-04-05	16	11184	N17W27	170	138	95
2011-04-06	16	11185	N23E36	100	37	28

12-minute interval. All AIA images should be corrected to a single pre-event exposure time (2.0 or 2.9 s) and divided by the CCF before the extraction of the arcade and dimming areas. Then, by coaligning the extracted areas with the HMI magnetogram, the corresponding erupted flux, Φ_{HMI} , is calculated.

Figure 4 Relationship between the MDI and HMI magnetic fluxes of the largest ARs over the period from 2010 May to 2011 April (see Table 2). The dotted line corresponds to $\Phi_{MDI} = 1.4\Phi_{HMI}$.



Possible magnitudes as well as the onset and peak times of a geomagnetic storm and Forbush decrease are estimated by means of conversion of the corresponding empirical expressions, obtained in Articles I and II for SOHO data, in accordance with the relation $\Phi_{MDI} = 1.4\Phi_{HMI}$. For SDO data, these expressions are as follows (again Φ_{HMI} is in units of 10^{20} Mx):

- GMS intensity (Dst and Ap indexes)

$$Dst [nT] = 30 - 15.4(\Phi_{HMI} + 3.8)^{1/2},$$

$$Ap [2nT] = 1.12\Phi_{HMI}.$$

- FD magnitude

$$A_F [\%] = -0.3 + 0.042\Phi_{HMI}.$$

- The onset (ΔT_o) and peak (ΔT_p) transit times, *i.e.* the intervals between the eruption time (maximum time of an associated soft X-ray burst) and the start and peak of a corresponding GMS

$$\Delta T_o [h] = 98/(1 + 0.00616\Phi_{HMI}),$$

$$\Delta T_p [h] = 118/(1 + 0.0056\Phi_{HMI}).$$

6. Examples

Now we consider some examples of an SDO-based post-diagnosis related to several large eruptions in ARs located not far from the solar disk center and to major GMSs that occurred during the current Solar Cycle 24. As already noted, as a result of the relatively low level of solar activity after 2009, only a few major GMSs with $Dst < -100$ nT occurred. Most of the GMSs were caused by filament eruptions outside ARs and sometimes by high-speed solar wind from coronal holes (Gopalswamy *et al.*, 2015; Gopalswamy, Tsurutani, and Yan, 2015). For instance, the strongest geomagnetic storm of the current solar cycle with a minimum $Dst = -228$ nT on 2015 March 17 was initiated by

a large south-west filament eruption near AR 12297. Note that according to our estimations, its erupted magnetic flux, $\Phi_{\text{HMI}} \approx 90.5 \times 10^{20}$ Mx (corresponding to the flux measured by MDI of $\Phi_{\text{MDI}} \approx 126.7 \times 10^{20}$ Mx), was higher than the fluxes in filament eruptions that caused the GMSs during Solar Cycle 23 (blue triangles in Figure 4 of Article I).

Table 3 presents the results of the SDO-based diagnosis of five flare-associated eruptions in ARs carried out according to the procedure described in the previous section. The table lists parameters of a solar event in the second to sixth columns, including the date, peak time, coordinates, and GOES class of a related flare (second to fifth columns), and a total unsigned magnetic flux calculated from HMI magnetograms in dimmings and arcades in the sixth column. The seventh to nineteenth columns are related to the geospace disturbance, including its peak date and time, and estimated (letter code “est”) and observed (“obs”) parameters of a corresponding GMS and FD. Information on the observed hourly Dst index was taken from the WDC2 Kyoto service (<http://wdc.kugi.kyoto-u.ac.jp/dstdir/index.html>), while the values of the three-hour Ap index were estimated in the GeoForschungsZentrum (GFZ) Potsdam (<ftp://ftp.gfz-potsdam.de/pub/home/obs/kp-ap/wdc/>). The onset transit time, ΔT_o , is defined as an arrival time of the corresponding interplanetary disturbance (shock wave) at Earth indicated by the geomagnetic storm sudden commencement (SSC) (<http://www.obsebre.es/en/rapid>). Following Article I, the FD maximum magnitude is adopted; this magnitude corresponds to a cosmic-ray rigidity of 10 GV evaluated from data of the world network of neutron monitors using the global survey method (Krymskii *et al.*, 1981; Belov *et al.*, 2005). Additionally, the eighteenth and nineteenth columns of Table 3 list the hourly strength of the total interplanetary magnetic field near the Earth, B_t , and its B_z component according to the Operating Missions as a Node on the Internet (OMNI) data (ftp://spdf.gsfc.nasa.gov/pub/data/omni/low_res_omni/).

Table 3 confirms the results of Articles I and II that the early diagnosis of the eruptions, based on the erupted magnetic flux evaluated in this case from SDO data, provides an approximate assessment for the importance of the related space weather disturbances. Particularly, the estimated values of Dst, Ap, ΔT_o , ΔT_p , and FD are comparable with the observed values. According to the NOAA space weather scale (<http://www.swpc.noaa.gov/noaa-scales-explanation>), four events (events 1–3 and 5) are classified as G2–G3 (moderate–strong) storms, and one (event 4) as G4 (severe) storm, judging from both the estimated and observed GMS intensity.

Table 3 presents an apparent scattered correspondence between the estimated and observed parameters of the GMSs and FDs. Indeed, the larger the erupted flux, the stronger the actual intensity of the GMSs and FDs and shorter the time intervals between the parent eruption and the GMS onset and peak. For example, the Pearson correlation coefficient between the estimated Dst and its observed value is 0.61. On average, $Dst_{\text{obs}}/Dst_{\text{est}} = 0.87 \pm 0.19$ ($\pm 22\%$), while the role of the B_z component seems to be comparable, $-B_z/B_t = 0.75 \pm 0.11$ ($\pm 15\%$). Thus, the differences between the estimated and observed Dst can be mostly due to the unaccounted B_z . There is also a close correspondence with a correlation coefficient of 0.91 between the erupted flux (sixth column) and the total magnetic field strength (B_t in the eighteenth column) brought to Earth by the ICMEs.

The event on 2016 June 21 (event 4 in Table 3) with the largest erupted flux resulted in the most intense GMS and FD; it also has the shortest transit times and strongest interplanetary magnetic field. In some events, for example events 1 and 2, the estimated GMS intensity, measured both by the Dst and Ap indexes, markedly exceeds the observed intensity, while the magnitudes of the FDs are much closer. The reason apparently is that in these cases the negative B_z component, which determines the GMS intensity, but which is not considered in our preliminary tool, amounts to only part of the total interplanetary magnetic strength, which determines the FD magnitude.

Table 3 Results of the SDO-based post-diagnosis of some eruptions of Solar Cycle 24.

No	Eruption Date	Time UT	Position	Flare class	Φ_{HMI} [10^{20} Mx]	Geomagnetic storm		Ap [2nT]		ΔT_o [h]		ΔT_p [h]		Forbush decrease [%]		Magnetic field [nT]	
						Peak dd/hh	Dst [nT]	est	obs	est	obs	est	obs	est	obs	B_t	B_z
1	2012-03-07	00:24	N17E27	X5.4	178.5	09/09	-178	200	132	47	35	59	56	7.2	11.7	23.1	-16.1
2	2012-07-12	16:49	S15W01	X1.4	197	15/19	-188	220	132	44	49	56	65	8.0	6.4	27.3	-17.7
3	2013-03-15	06:58	N11E12	M1.1	85.5	17/21	-116	96	111	64	47	80	62	3.3	4.6	17.8	-14
4	2015-06-21	02:06	N12E13	M2.6	234.4	23/05	-208	263	236	40	40	51	52	9.5	8.4	37.7	-26.3
5	2015-12-28	12:45	N19W22	M1.8	128.3	01/01	-147	144	80	55	63	69	84	5.1	4.3 ^a	16.9	-15.8

^aThe observed FD magnitude was evaluated from data of two high-latitude different-hemisphere stations, Thule and McMurdo.

As for the temporal parameters of GMSs, a close correspondence between the estimated and observed values of both ΔT_o and ΔT_p is present for event 4. In other cases, some differences can be seen. Our simple tentative estimates were made as if they were issued right after an eruption, without taking into account preceding activity, actual distributions of the magnetic field and plasma in the corona, ICME drag in the solar wind, and other factors.

7. Concluding Remarks

We compared quantitative parameters of CME-associated post-eruption arcades and dimmings observed with EUV telescopes and magnetographs onboard the SOHO and SDO spacecraft. Two basic facts have been established. First, with the adopted thresholds of relative brightness changes, practically the same arcade and dimming areas are extracted from EIT 195 Å and AIA 193 Å images, if their cross-calibration factor in a range of 3.6–5.8 and 5.0–8.2 is taken into account for the AIA exposure time 2.0 and 2.9 s, respectively. Second, for the same photospheric areas of strong magnetic fields in large active regions, the MDI line-of-sight magnetic flux systematically exceeds the HMI flux by a factor of 1.4.

These results allowed us to upgrade the tool for the early diagnostics of AR eruptions described in Articles I and II for SOHO data to the current SDO observations. Empirical relationships are obtained to connect the erupted magnetic flux measured from SDO data with possible intensity and temporal parameters of forthcoming non-recurrent GMSs and FDs. The case studies presented here confirm that the updated diagnostic tool based on SDO data also produces acceptable results, providing a prompt and sufficiently correct assessment of the importance of forthcoming space weather disturbances using only magnetic flux within the arcade and dimming areas. The tool presented here and previously in Articles I and II corroborates the idea that parameters of solar eruptions, CMEs and ICMEs, and geospace disturbances are largely determined not only by the characteristics of associated ARs and flares, but by a measurable quantity as this erupted magnetic flux in arcades and dimmings (see Article I; Démoulin, 2008; Mandrini *et al.*, 2009 for a review).

It is clear, however, that the proposed tool for the early preliminary prognostic estimations does not take into account many factors affecting the GMS and FD characteristics. Consequently, as in Articles I and II, we do not pursue exact estimates of the parameters of GMSs and FDs and focus instead on their possible importance. In practice, our tool should be the starting point of a complex of comprehensive forecasting tools, which would consider information on near-the-Sun CMEs, various models of eruptions and drag of ICMEs propagating in the solar wind, stereoscopic observations, estimation of a probable sign of the B_z component, and others (see, *e.g.*, Gopalswamy, Tsurutani, and Yan, 2015, and references therein).

Acknowledgements We appreciate the painstaking work of the anonymous reviewer for valuable remarks and recommendations that significantly helped us to bring this article to its final form. The authors thank the SOHO/EIT and MDI and SDO/AIA and HMI teams for their open data used in our study. SOHO is a project of international cooperation between ESA and NASA. SDO is a mission of the NASA's Living With a Star (LWS) Program. We are grateful to A.V. Belov for his assistance and useful discussions. This research was partially supported by the Russian Foundation of Basic Research under grant 14-02-00367.

Disclosure of Potential Conflicts of Interest The authors claim that they have no conflicts of interest.

References

Belov, A.V.: 2009, *Proc. IAU Symp.* **257**, 439. DOI.

- Belov, A., Baisultanova, L., Eroshenko, E., Mavromichalaki, H., Yanke, V., Pchelkin, V., *et al.*: 2005, *J. Geophys. Res.* **110**, A09S20. DOI.
- Bothmer, V., Zhukov, A.: 2007, In: Bothmer, V., Daglis, I.A. (eds.) *Space Weather – Physics and Effects* **31**. DOI.
- Cane, H.V.: 2000, *Space Sci. Rev.* **93**, 55. DOI.
- Chertok, I.M., Grechnev, V.V.: 2005, *Solar Phys.* **229**, 95. DOI.
- Chertok, I.M., Grechnev, V.V., Belov, A.V., Abunin, A.A.: 2013, *Solar Phys.* **282**, 175. DOI (Article I).
- Chertok, I.M., Abunina, M.A., Abunin, A.A., Belov, A.V., Grechnev, V.V.: 2015, *Solar Phys.* **290**, 627. DOI (Article II).
- Couvidat, S., Schou, J., Hoeksema, J.T., Bogart, R.S., Bush, R.I., Duvall, T.L.: 2016, *Solar Phys.* **291**, 1887. DOI.
- Démoulin, P.: 2008, *Ann. Geophys.* **26**, 3113. DOI.
- Delaboudinière, J.-P., Artzner, G.E., Brunaud, J., Gabriel, A.H., Hochedez, J.F., Millier, F., *et al.*: 1995, *Solar Phys.* **162**, 291. DOI.
- Domingo, V., Fleck, B., Poland, A.I.: 1995, *Solar Phys.* **162**, 1. DOI.
- Gopalswamy, N., Tsurutani, B., Yan, Y.: 2015, *Prog. Earth Planet. Sci.* **2**, 13. DOI.
- Gopalswamy, N., Yashiro, S., Xie, H., Akiyama, S., Mäkelä, P.: 2015, *J. Geophys. Res.* **120**, 9221. DOI.
- Gosling, J.T.: 1993, *J. Geophys. Res.* **113**, 18937. DOI.
- Grechnev, V.V., Lesovoi, S.V., Smolkov, G.Y., Krissinel, B.B., Zandanov, V.G., Altyntsev, A.T., Kardapolova, N.N., Sergeev, R.Y., Uralov, A.M., Maksimov, V.P., Lubyshev, B.I.: 2003, *Solar Phys.* **216**, 239. DOI.
- Hanaoka, Y., Shibasaki, K., Nishio, M., Enome, S., Nakajima, H., Takano, T., Torii, C., Sekiguchi, H., Bushimata, T., Kawashima, S., Shinohara, N., Irimajiri, Y., Koshiishi, H., Kosugi, T., Shiomi, Y., Sawa, M., Kai, K.: 1994, *Proc. Kofu Symp.* 35.
- Harra, L.K., Mandrini, C.H., Dasso, S., Gulisano, A.M., Steed, K., Imada, S., *et al.*: 2011, *Solar Phys.* **268**, 213. DOI.
- Hudson, H.S., Cliver, E.W.: 2001, *J. Geophys. Res.* **106**, 25199. DOI.
- Kahler, S.: 1977, *Astrophys. J.* **214**, 891. DOI.
- Kochanov, A.A., Anfinogentov, S.A., Prosovetsky, D.V., Rudenko, G.V., Grechnev, V.V.: 2013, *Publ. Astron. Soc. Japan* **65**. DOI.
- Krymskii, G.F., Kuz'min, A.I., Krivoshapkin, P.A., Samsonov, I.S., Skripin, G.V., Transkij, I.A., Chirkov, N.P.: 1981, *Kosmicheskie luchi i solnechnyi veter (Cosmic Rays and Solar Wind)*, Nauka, Novosibirsk.
- Lemen, J.R., Title, A.M., Akin, D.J., Boerner, P.F., Chou, C., Drake, J.F., *et al.*: 2012, *Solar Phys.* **275**, 17. DOI.
- Liu, Y., Hoeksema, J.T., Scherrer, P.H., Schou, J., Couvidat, S., Bush, T.L., *et al.*: 2012, *Solar Phys.* **279**, 295. DOI.
- Mandrini, C.H., Nakwacki, M.S., Attrill, G., van Driel-Gesztelyi, L., Dasso, S., Démoulin, P.: 2009, In: Gopalswamy, N., Webb, D.F. (eds.) *Universal Heliospheric Processes, IAU Symp.* **257**, 265. DOI.
- Miklenic, C.H., Veronig, A.M., Vršnak, B.: 2009, *Astron. Astrophys.* **499**, 893. DOI.
- Pesnell, W.D., Thompson, B.J., Chamberlin, P.C.: 2012, *Solar Phys.* **275**, 3. DOI.
- Qiu, J., Hu, Q., Howard, T.A., Yurchyshyn, V.B.: 2007, *Astrophys. J.* **659**, 758. DOI.
- Reinard, A.A., Biesecker, D.A.: 2008, *Astrophys. J.* **674**, 576. DOI.
- Reinard, A.A., Biesecker, D.A.: 2009, *Astrophys. J.* **705**, 914. DOI.
- Richardson, I.G., Cane, H.V.: 2011, *Solar Phys.* **270**, 609. DOI.
- Riley, P., Ben-Nun, M., Linker, J.A., Mikic, Z., Svalgaard, L., Harvey, J., *et al.*: 2014, *Solar Phys.* **289**, 769. DOI.
- Scherrer, P.H., Bogart, R.S., Bush, R.I., Hoeksema, J.T., Kosovichev, A.G., Schou, J., *et al.*: 1995, *Solar Phys.* **162**, 129. DOI.
- Scherrer, P.H., Schou, J., Bush, R.I., Kosovichev, A.G., Bogart, R.S., Hoeksema, J.T., *et al.*: 2012, *Solar Phys.* **275**, 207. DOI.
- Sterling, A.C., Hudson, H.S., Thompson, B.J., Zarro, D.: 2000, *Astrophys. J.* **532**, 628. DOI.
- Svalgaard, L., Sun, X.: 2016. <http://hmi.stanford.edu/hminuggets/?p=1510>.
- Thompson, B.J., Plunkett, S.P., Gurman, J.B., Newmark, J.S., St. Cyr, O.C., Michels, D.J.: 1998, *Geophys. Res. Lett.* **25**, 2465. DOI.
- Tripathi, D., Bothmer, V., Cremades, H.: 2004, *Astron. Astrophys.* **422**, 337. DOI.
- Uralov, A.M., Grechnev, V.V., Rudenko, G.V., Myshyakov, I.I., Chertok, I.M., Filippov, B.P., Slemzin, V.A.: 2014, *Solar Phys.* **289**, 3747. DOI.
- Watson, F.T., Penn, M.J., Livingston, W.: 2014, *Astrophys. J.* **787**, 22. DOI.
- Yashiro, S., Gopalswamy, N., Mäkelä, P., Akiyama, S.: 2013, *Solar Phys.* **284**, 5. DOI.